# Improved quantum molecular dynamics model and its applications to fusion reaction near barrier

Ning Wang,[1,*] Zhuxia Li,[1,2,3,†] and Xizhen Wu[1,2,†]
[1]*China Institute of Atomic Energy, P. O. Box 275(18), Beijing 102413, People's Republic of China*
[2]*Nuclear Theory Center of National Laboratory of Heavy Ion Accelerator, Lanzhou 730000, People's Republic of China*
[3]*Institute of Theoretical Physics, Chinese Academy of Sciences, Beijing 100080, People's Republic of China*
(Received 18 October 2001; published 28 May 2002)

An improved quantum molecular dynamics model is developed. By using this model, the properties of ground state of nuclei from $^{6}$Li to $^{208}$Pb are described very well with one set of parameters. The fusion reactions for $^{40}$Ca+ $^{90}$Zr, $^{40}$Ca+ $^{96}$Zr, and $^{48}$Ca+ $^{90}$Zr at energies near the barrier are studied by this model. The experimental data of the fusion cross sections for $^{40}$Ca+ $^{90,96}$Zr at energies near the barrier are reproduced remarkably well without introducing any new parameters. The mechanism for the enhancement of the fusion cross sections for neutron-rich nuclear reaction near barrier is analyzed.

DOI: 10.1103/PhysRevC.65.064608 PACS number(s): 25.70.−z, 24.10.−i

## I. INTRODUCTION

Heavy-ion fusion reactions at energies below and near the Coulomb barrier have received considerable attention recently (for example, see [1–7] and references therein). Of special interest are the dynamical mechanisms for the enhancement of the fusion cross section for neutron-rich nuclear reactions at energies near the barrier, such as the deformation of the target and projectile before contact, the neck formation, and the particle transfer after contact. The quantum molecular dynamics (QMD) model has been widely used in intermediate energy heavy-ion collisions, and successfully provides much dynamic information about the reaction mechanism (for example, see [8–10]). It would be of great significance if the QMD model could be applied to study the dynamical mechanism of heavy-ion fusion at energies near the barrier. However, it is still of difficulties to apply the QMD model to low-energy reactions. One of the main difficulties is that one has to deal with the problem of the time evolution of nuclear many-body systems which are of fermionic nature. On a quantum-mechanical level, the wave function must be antisymmetrized because of the fermionic nature of the nuclear constituents. In antisymmetrized molecular dynamics (AMD) [11] and fermionic molecular dynamics (FMD) [12] the wave function of the system is expressed by a Slater determinent of $N$ wave packets. AMD and FMD made a great achievement in describing the nuclear reaction and structure for light nuclei. Nevertheless, for AMD and FMD one has to deal with the time evolution of at least $N!$ terms, which would be computationally very demanding, and the CPU time necessary to work out calculations for heavy systems is very large for practical studies [13]. In the QMD model, each nucleon is represented by a coherent state, and the total $N$-body wave function is assumed to be the direct product of coherent states. Therefore, the QMD calculations are very practical for studying the heavy systems. Obviously, the QMD model lacks a fermionic nature due to the neglect of antisymmetrization, although two-body collisions with Pauli blocking have some effects on maintaining part of the fermionic feature of systems. In fact, two-body collisions are very rare in ground states or in fusion reactions. To compensate for this shortcoming, the two-body Pauli potential was introduced by several authors [14–18] to mimic the Pauli principle. The Pauli potential can improve the ground states to a certain extent, but it causes undesirable problems which may destroy the initial phase-space distribution obtained according to the nuclear ground state after a long time. In constrained quantum molecular dynamics (CoMD), Papa *et al.* proposed a phase-space density constraint [13] with which this problem has been partly overcome.

Concerning the wave-packet width in FMD and EQMD [19] models the width is dynamic, and in the normal QMD model it is a constant. But the values of width in the QMD calculations are quite different. For example, in [10] the Gaussian wave packet width was taken as $L=4.33$ fm$^2$ for reaction Ca+Ca and $L=8.66$ fm$^2$ for Au+Au. In Ref. [20] the authors took two different values of the width of the Gaussian wave packet for multifragmentation and fusion reaction in order to have reasonable results. Therefore, it seems to us that it is worthwhile to make a further study of the influence of the wave-packet width on the ground-state properties of individual nuclei and the Coulomb barrier in fusion reactions. For this study we propose a system-size-dependent wave-packet width.

Aiming at studying the dynamical process of fusion reactions at energies near the barrier one will face difficulties by using the normal QMD mode, and one needs a model which can describe not only the ground-state properties of individual nuclei at initial time well but also their time evolution, and which furthermore can provide a reasonable Coulomb barrier for fusion reaction. In this work we develop an improved QMD model by introducing series improvements, and then make careful tests of the model. We expect that our model can meet the requirement of studying the dynamical process of fusion reaction at energies near the barrier. The structure of this paper is as follows: In the Sec. II, we introduce our improved QMD model. Then we make an application of this model to describing the nuclear ground state and the fusion reaction process in Sec. III. Finally a short summary and conclusion is given in Sec. IV.

*Email address: wangning@iris.ciae.ac.cn
†Email address: lizwux@iris.ciae.ac.cn

 

## II. IMPROVED QMD MODEL

In this section we introduce the improved QMD model in more detail. First, a brief introduction to QMD model is presented. Then, the main improvements are introduced and their effects are analyzed. Finally, the preparation procedure of initial nuclei is given.

### A. Brief introduction to the QMD model

In the QMD model, each nucleon is represented by a coherent state of a Gaussian wave packet,

$$\phi_i(\mathbf{r}) = \frac{1}{(2\pi\sigma_r^2)^{3/4}} \exp\left[ -\frac{(\mathbf{r}-\mathbf{r}_i)^2}{4\sigma_r^2} + \frac{i}{\hbar}\mathbf{r}\cdot\mathbf{p}_i \right], \tag{1}$$

where $\mathbf{r}_i$ and $\mathbf{p}_i$ are the centers of the $i$th wave packet in the coordinate and momentum space, respectively. $\sigma_r$ represents the spatial spread of the wave packet. The total $N$-body wave function is assumed to be the direct product of these coherent states. Through a Wigner transformation of the wave function, the $N$-body phase-space distribution function is given by

$$f(\mathbf{r},\mathbf{p}) = \sum_i \frac{1}{(\pi\hbar)^3} \exp\left[ -\frac{(\mathbf{r}-\mathbf{r}_i)^2}{2\sigma_r^2} - \frac{2\sigma_r^2}{\hbar^2}(\mathbf{p}-\mathbf{p}_i)^2 \right]. \tag{2}$$

The density and momentum distributions of a system read

$$\rho(\mathbf{r}) = \int f(\mathbf{r},\mathbf{p}) d^3p = \sum_i \rho_i(\mathbf{r}), \tag{3}$$

$$g(\mathbf{p}) = \int f(\mathbf{r},\mathbf{p}) d^3r = \sum_i g_i(\mathbf{p}), \tag{4}$$

respectively, where the sum runs over all particles in the system. $\rho_i(\mathbf{r})$ and $g_i(\mathbf{p})$ are the density and momentum distributions of nucleon $i$:

$$\rho_i(\mathbf{r}) = \frac{1}{(2\pi\sigma_r^2)^{3/2}} \exp\left[ -\frac{(\mathbf{r}-\mathbf{r}_i)^2}{2\sigma_r^2} \right], \tag{5}$$

$$g_i(\mathbf{p}) = \frac{1}{(2\pi\sigma_p^2)^{3/2}} \exp\left[ -\frac{(\mathbf{p}-\mathbf{p}_i)^2}{2\sigma_p^2} \right], \tag{6}$$

where $\sigma_r$ and $\sigma_p$ are the widths of wave packets in coordinate and momentum space, respectively, and they satisfy the minimum uncertainty relation

$$\sigma_r\sigma_p = \frac{\hbar}{2}. \tag{7}$$

In the QMD model, the nucleons in a system move under a self-consistently generated mean field, and the time evolution of $\mathbf{r}_i$ and $\mathbf{p}_i$ is governed by Hamiltonian equations of motion

TABLE I. The parameters adopted in the present work.

| $\alpha$(GeV) | $\beta$(GeV) | $\rho_0$(fm$^{-3}$) | $g_0$(GeV fm$^{-5}$) | $C_s$(GeV) |
|---|---|---|---|---|
| −0.124 | 0.071 | 0.165 | 0.96 | 0.032 |

$$\dot{\mathbf{r}}_i = \frac{\partial H}{\partial \mathbf{p}_i}, \quad \dot{\mathbf{p}}_i = -\frac{\partial H}{\partial \mathbf{r}_i}. \tag{8}$$

The Hamiltonian $H$ consists of the kinetic energy and the effective interaction potential energy:

$$H = T + U, \tag{9}$$

$$T = \sum_i \frac{\mathbf{p}_i^2}{2m}. \tag{10}$$

The effective interaction potential energy includes the nuclear local interaction potential energy and Coulomb interaction potential energy:

$$U = U_{loc} + U_{coul} \tag{11}$$

and

$$U_{loc} = \int V_{loc} d^3\mathbf{r}. \tag{12}$$

$V_{loc}$ is the potential energy density, which can be derived directly from a zero-range Skyrme interaction [14,21], and it reads

$$V_{loc} = \frac{\alpha}{2}\frac{\rho(\mathbf{r})^2}{\rho_0} + \frac{\beta}{3}\frac{\rho(\mathbf{r})^3}{\rho_0^2} + \frac{C_s}{2}\frac{[\rho_p(\mathbf{r})-\rho_n(\mathbf{r})]^2}{\rho_0} + \frac{g_1}{2}[\nabla\rho(\mathbf{r})]^2. \tag{13}$$

By using

$$\langle Q \rangle_i = \int \rho_i(\mathbf{r}) Q d^3\mathbf{r}, \tag{14}$$

the nuclear local interaction potential energy can be written as

$$U_{loc} = \frac{\alpha}{2}\sum_i \left\langle \frac{\rho}{\rho_0} \right\rangle_i + \frac{\beta}{3}\sum_i \left\langle \frac{\rho^2}{\rho_0^2} \right\rangle_i + \frac{C_s}{2}\int \frac{(\rho_p-\rho_n)^2}{\rho_0} d^3\mathbf{r} + \int \frac{g_1}{2}(\nabla\rho)^2 d^3\mathbf{r}. \tag{15}$$

Because of the Gaussian form of density distribution in Eq. (5), all of the integrals in Eq. (12) can be done analytically; furthermore all but one of the sums involves only $N^2$

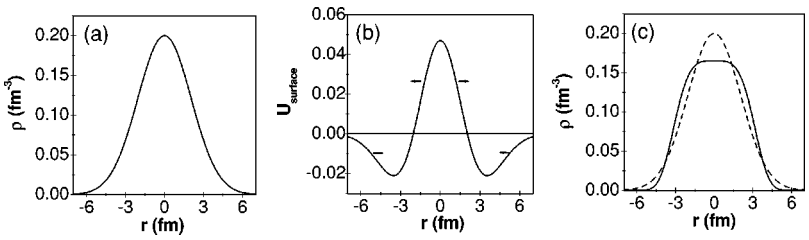


FIG. 1. The schematic figure of the effect of the surface energy term. (a) The density distribution of Boltzmann form, (b) The shape of the surface energy term; the arrows denote the direction of corresponding force. (c) The comparison between the density distributions calculated with (solid curve) and without (dashed curve) the surface energy term taken into account, respectively.

terms. The problem in Eq. (15) is that $\Sigma_i\langle\rho^2/\rho_0^2\rangle_i$ is of order of $N^3$, and, for a system of hundreds of particles, an evaluation of $N^3$ elements is very time consuming and computationally prohibitive, so it is approximated by [14]

$$\sum_i \left\langle \frac{\rho^2}{\rho_0^2} \right\rangle_i \approx \sum_i \left\langle \frac{\rho}{\rho_0} \right\rangle_i^2 + \int \frac{g_2}{2}(\nabla\rho)^2 d^3\mathbf{r}, \qquad (16)$$

which is a $N^2$ operation. Since the second term in Eq. (16) has the same functional form as the surface energy term in Eq. (15), we combine them into one term and call it the surface energy term with parameter $g_0 = g_1 + g_2$. The Coulomb potential energy is obtained from

$$U_{coul} = \frac{1}{2}\sum_{i\neq j} \int \rho_i(\mathbf{r}) \frac{e^2}{|\mathbf{r}-\mathbf{r}'|} \rho_j(\mathbf{r}') d^3\mathbf{r} d^3\mathbf{r}'. \qquad (17)$$

Concerning the collision term, the treatment of isospin-dependent Pauli blocking is introduced (see Ref. [22]),which is especially useful for reactions of heavy nuclear systems. The parameters in this work are listed in Table I.

### B. Effect of the surface energy term and the phase-space density constraint

It is obvious that surface effects are important for a finite system. Let us first study the effects of the term $U_{surface} = (g_0/2)\int(\nabla\rho)^2 d^3r$ schematically. In Fig. 1, we show a schematic figure of the effect of the surface energy term. As mentioned in Sec. I, the initial density distribution of a system will evolve to a classical one after a long time according to the classical equations of motion. Suppose we have a Gaussian form of density distribution as shown in Fig. 1(a). With this density distribution, the surface energy term $U_{surface}$ is obtained by definition, and its shape is shown in Fig. 1(b). From the figure we can see that the particles in the central region experience a repulsion and are forced to move toward the outside. Thus the density at the central region is refrained from evolving to an unreasonably high value. The particles at the surface ''feel'' an attraction, and move toward the inside so that the surface diffuseness of the density distribution will not be too large. Figure 1(c) shows the influence of the surface energy term on the density distribution. The solid and dashed curves are the density distribution calculated with and without the surface term taken into account, respectively. It is clear that the density distribution calculated with the surface term is more reasonable than that without the surface term.

For illustrating the effect of the surface term on the realistic nuclear system, in Figs. 2 and 3 we show the time evolution of the density distribution of $^{90}$Zr calculated without and with the surface term taken into account. The initial density distribution is obtained by relativistic mean field (RMF) theory calculations [23]. When the surface energy term is not included, as shown in Fig. 2, the density distribution can be kept stable and the central density can maintain a value lower than 0.2 fm$^{-3}$ only at the early stage [for example, see Fig. 2 (subfigure 1)]. With further time evolution, the density distribution changes and deviates from the initial one. The central density grows gradually and at about $t = 400$ fm/$c$ [see Fig. 2 (subfigure 3)] the central density even reaches 0.3 fm$^{-3}$. After $t = 400$ fm/$c$ the spurious emission of nucleons appears while the central density is still too high. When the surface energy term is included, as shown in Fig. 3, with time evolution the density distribution is remarkably stable and its shape is kept the same as the initial one. Even at $t = 800$ fm/$c$ [see Fig. 3 (subfigure 4)], the central density still remains the same value of $\rho = 0.165$ fm$^{-3}$ as that at the initial time, and we find the shape of the density distribution does not change even for much longer times. From the comparison of these two figures, one can clearly see that the surface energy term is effective to maintain a reasonable density distribution for ground state of an individual nucleus during the time evolution.

The momentum distribution will evolve to a classical distribution from initial momentum distribution after a long time, as mentioned in Sec. I. To avoid this, we introduce the

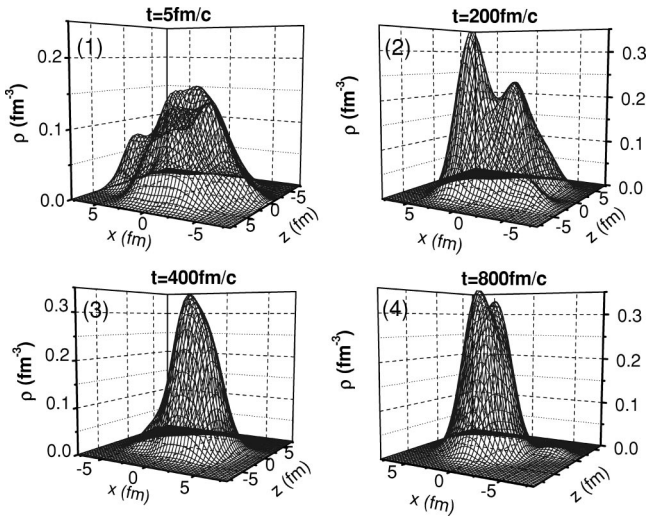


FIG. 2. The time evolution of the density distribution of $^{90}$Zr without the surface energy term taken into account.

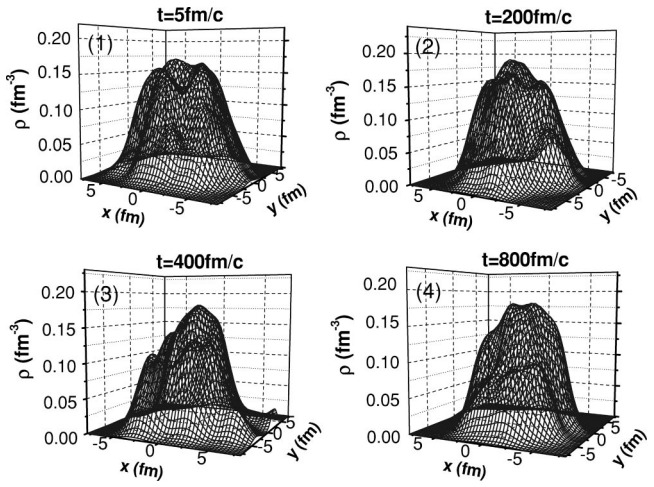


FIG. 3. The same as Fig. 2, but with the surface energy term taken into account.

phase-space density constraint of the CoMD model proposed by Papa *et al.* [13] into our model. We make a test for the effect of the phase-space density constraint on the time evolution of the momentum space distribution. We find that this kind of constraint affects the low momentum part of the momentum distribution strongly, and thus it can effectively restrain the number of particles with low momentum from being too large. Figure 4 shows a comparison of the time evolution of the average momentum distribution calculated without taking the constraint (dashed curves) and with taking the constraint (solid curves) for 200 $^{208}$Pb nuclei. Here the momentum distribution means the distribution of the centroid momentums of wave packets of nucleons in a system. From the figure one can see that at the initial time, the momentum distribution (dash-dotted curves) is reasonable. With time evolution, the difference in the momentum distributions between these two cases becomes obvious. When the phase-space density constraint is not taken into account, the number of particles with low momentum increases greatly, and the momentum distribution deviates from the initial one obviously, as shown by the dashed curves. This problem is usually ignored in the QMD calculations for intermediate- and high-energy heavy-ion reactions. For describing the ground state or fusion reactions near barrier, however, this problem should be considered seriously. From the solid curves one can find that the behavior of the time evolution of the momentum distribution, especially the low momentum part, is improved a lot after taking the phase-space density constraint into account. We note that the high-momentum part of the distribution has too large diffuseness comparing with the initial one. This means that the phase-space constraint is still not enough in controlling the momentum distribution to be as good as request. But even so we find that it improves the fusion reaction near the barrier very much. An investigation of further improvements in the behavior of the time evolution of the momentum distribution is in progress.

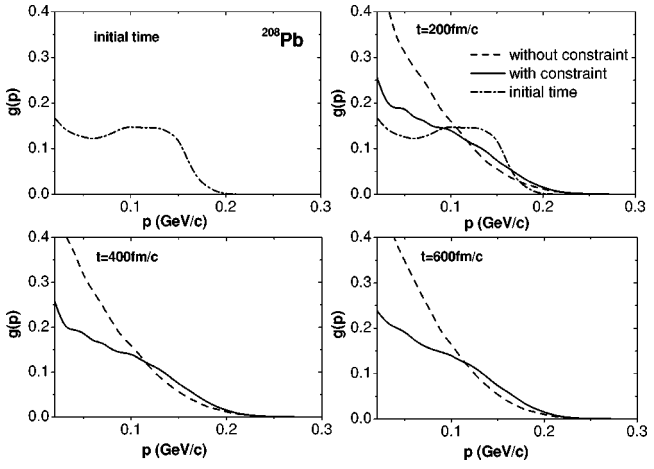


FIG. 4. The time evolution of the momentum distribution of $^{208}$Pb. The dash-dotted curves denote the initial momentum distribution obtained from the relativistic mean-field calculations. The dashed and solid curves denote the momentum distribution without and with the phase-space density constraint taken into account, respectively.

### C. System-size-dependent wave-packet width

It is understood that the wave-packet width in the QMD model can be regarded as a quantity having relations with the interaction range of a particle. For finite systems, particles should be localized in a finite size corresponding to the size of the system, and thus the wave-packet width should have some relations with the range of the mean field which binds particles together. In practice, one already notes that the value of the wave-packet width affects the calculation results obviously, so that one usually makes an adjustment to a certain extent. For example, in Ref. [10] the wave-packet width is taken to be $\sigma_r = 1.04$ fm for Ca+Ca and $\sigma_r = 1.47$ fm (i.e., $L = 8.66$ fm$^2$ in the notation of Ref. [10]) for Au+Au. As is well known, the stability of projectile and target nuclei in QMD calculations is a basic requirement for studying the fusion reaction at energies near the barrier. Here let us make an investigation in the influence of the wave-packet width on the stability of the ground state of an individual nucleus. As an example, for the ground state of $^{208}$Pb, we show the time evolution of its density distribution in Figs. 5(a) and 5(b), with the wave-packet widths taken to be $\sigma_r = 1.04$ and 1.44 fm, respectively. One can see from the figures that for the $\sigma_r = 1.44$ fm case the system is stable with no particle emission, and simultaneously both the density and momentum distribution are reasonable. For $\sigma_r = 1.04$ fm case the system becomes unstable even at an early time $t = 150$ fm/$c$ [see Fig. 5(a) (Fig. 2)] and there is a spurious emission of about 30 particles until 800 fm/$c$. It is because too small a $\sigma_r$ corresponds to too large a $\sigma_p$, which leads to too large an average kinetic energy per nucleon. In describing heavy-ion reactions, if spurious emission becomes serious, the results will become invalid. Therefore, in Ref. [10], a larger wave-packet width for the Au+Au case and a smaller width for Ca+Ca case were taken. This treatment seems to us to be reasonable.

For light nuclei, let us look at Fig. 6, which shows the time evolution of the root-mean-square radius of $^{40}$Ca for $\sigma_r = 1.3$ and 1.04 fm. The figure demonstrates that if too

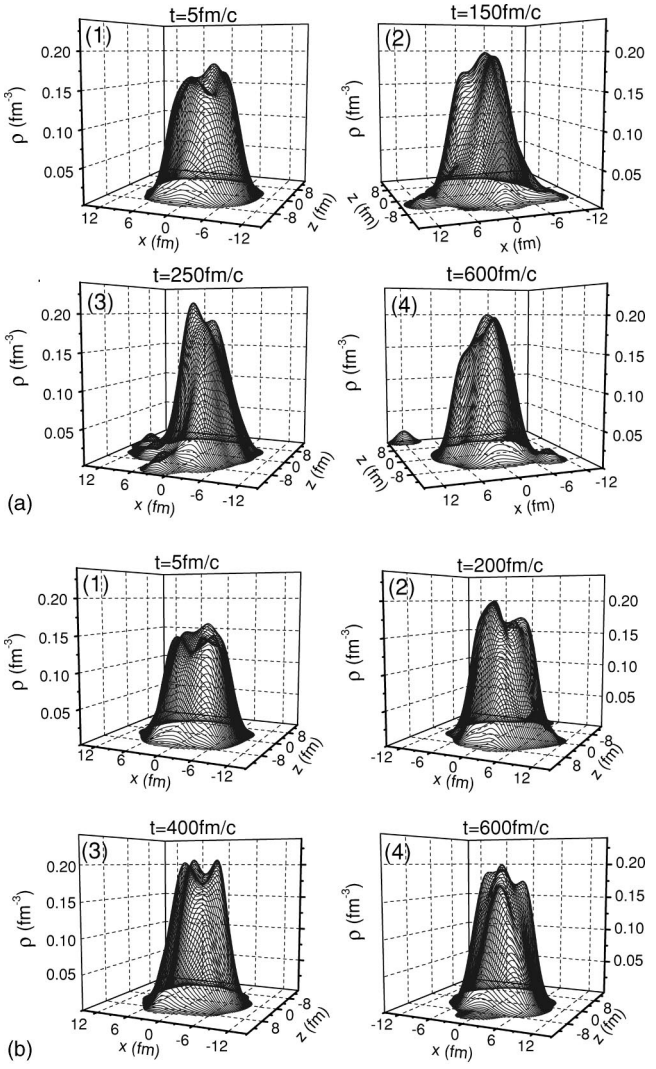


FIG. 5. The time evolution of the density distribution of $^{208}$Pb with the wave-packet width taken to be (a) $\sigma_r = 1.04$ fm and (b) $\sigma_r = 1.44$ fm.

large a wave-packet width is used the fluctuation of the average root-mean-square radius will become large because of the too large localization region. A large fluctuation of the root-mean-square radius means the instability of a nucleus and it should be avoided.

Based on the above discussion we propose a system-size-dependent wave packet width

$$\sigma_r = 0.16N^{1/3} + 0.49, \tag{18}$$

where $N$ is the number of nucleons bound in the system. We will show in Sec. III A that after introducing the system-size-dependent wave-packet width, our model is able to describe the bulk properties of nuclei in a wide mass region from $^{6}$Li to $^{208}$Pb. In order to introduce the system-size-dependent wave-packet width into heavy-ion reaction process, in each time evolution step for each particle we have to check how many particles are bound together with this particle to seek the size of the system to which the particle belongs. For heavy-ion fusion reactions, the projectile and target have

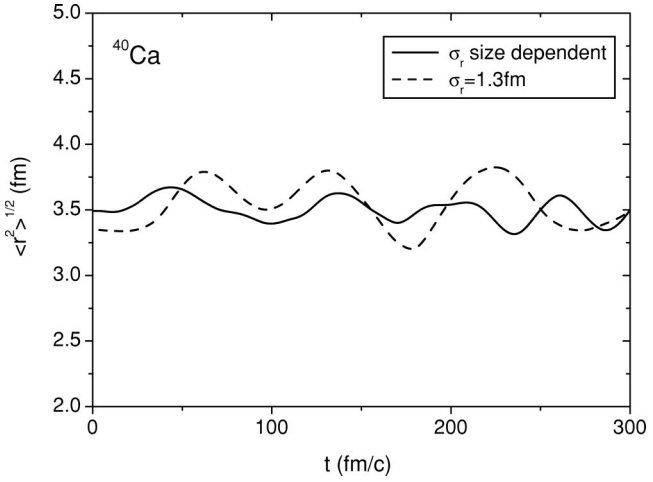


FIG. 6. The time evolution of the root-mean-square radius of $^{40}$Ca with the system-size-dependent wave-packet width (solid curve) and the fixed width $\sigma_r = 1.3$ fm (dashed curve).

their own wave-packet widths before contact; after contact to projectile and target gradually melt into one system, and consequently all particles have a common width. In Sec. III B, we will show the importance of taking a system-size-dependent wave-packet width into account in describing the Coulomb barrier.

### D. Preparation of initial nuclei

As is well known, the initial condition is very important in QMD calculations. In the present work, the preparation of initial nuclei is as the following: First, the neutron and proton density distributions of the nuclei are obtained by means of RMF calculations. Then the positions of each nucleon in nuclei are sampled according to the density distribution obtained. Second, based on the density distribution given by expression (5), the local Fermi momentum $P_F$ is obtained by the local-density approximation. Considering that the momentum of each nucleon is also represented by a wave packet with a width of $\sigma_p$ which satisfies the minimum uncertainty relation $\sigma_r \sigma_p = \hbar/2$, the local Fermi momentum $P_F'$ used in sampling the momentums of nucleons should be smaller than $P_F$. The difference $\Delta P_F = P_F - P_F'$ should be roughly equal to the width at the half height of the Gaussian wave packet in momentum space [see expression (6)]. For light nuclei (the mass is smaller than 16) we make a slight adjustment of $\Delta P_F$ which is less than a tenth of $\Delta P_F$. The other procedures are similar with the normal QMD model in making preprepared nuclei. To check the stability of the preprepared initial nuclei, we let the preprepared nuclear systems evolve for at least 600 fm/$c$; then the ground state properties, including the root-mean-square radius, the binding energy, the density distribution, the momentum distribution, the phase-space distribution, etc. are checked elaborately. Only those preprepared nuclei for which the bulk properties and their time evolution are good enough, and there is no spurious particle emission for a long enough time, are selected as ''good initial nuclei.'' They are stored for usage in simulating reactions.

TABLE II. The binding energies per nucleon and root-mean-square radii for the ground state of selected nuclei from $^{6}$Li to $^{208}$Pb. The binding energies are compared with experimental data. The root-mean-square radii are compared with those obtained from the empirical formula [24].

| Nuclear name | Binding energy | | Mean-square radius | |
|---|---|---|---|---|
| | QMD | Exp. | QMD | Data |
| $^{6}$Li | 5.78 | 5.33 | 2.13 | 2.07 |
| $^{16}$O | 8.01 | 7.97 | 2.85 | 2.64 |
| $^{30}$P | 8.32 | 8.35 | 3.35 | 3.12 |
| $^{40}$Ca | 8.55 | 8.55 | 3.54 | 3.38 |
| $^{90}$Zr | 8.57 | 8.71 | 4.25 | 4.25 |
| $^{108}$Ag | 8.41 | 8.50 | 4.47 | 4.48 |
| $^{144}$Nd | 8.25 | 8.27 | 4.84 | 4.87 |
| $^{197}$Au | 8.01 | 7.92 | 5.30 | 5.35 |
| $^{208}$Pb | 7.87 | 7.87 | 5.41 | 5.43 |

## III. RESULTS

### A. Properties of the ground state

In Table II we give the calculated results of binding energies and root-mean-square radii for ground states of $^{6}$Li,$^{16}$O,$^{30}$P, $^{40}$Ca,$^{90}$Zr,$^{108}$Ag, $^{144}$Nd,$^{197}$Au, and $^{208}$Pb. The binding energies are compared with experimental data, and the root-mean-square radii are compared with those obtained from the empirical formula [24]

$$\langle r^2\rangle^{1/2}=0.82A^{1/3}+0.58. \tag{19}$$

One can see that the calculated binding energies are in good agreement with experimental data, and the root-mean-square radii are also in good agreement with empirical values obtained from Eq. (19) except for small nuclei. For small nuclei, our results are a little bit better than the empirical formula when we compare them with experimental data (see Ref. [12]). Considering how few parameters we use in this model, the obtained results in describing the ground-state properties of nuclei are quite satisfied. In addition to the static properties of the ground state of nuclei the behavior of time evolution of those quantities are also very concerned. In Fig. 7 we show the time evolution of the binding energies and root-mean-square radii for $^{16}$O, $^{40}$Ca, $^{90}$Zr, and $^{208}$Pb. One can see that their binding energies and root-mean-square radii remain constant with a very small fluctuation for a long enough time. One can further find, that the larger the size of a nucleus is, the smaller the fluctuations of the binding energy and mean square root of the radius with time evolution are which is because the mean field effect becomes stronger as the system size increases.

### B. Coulomb barrier

The Coulomb barrier plays a very important role in describing fusion reactions. Its height and width are two sensitive quantities in WKB calculations for fusion cross sections. In the QMD model, the Coulomb barrier is calculated microscopically by using the expressions

$$V_b(r)=\int d^3r_1\int d^3r_2\rho_1(\mathbf{r}_1-\mathbf{r}_{1c})V(\mathbf{r}_1-\mathbf{r}_2)\rho_2(\mathbf{r}_2-\mathbf{r}_{2c}), \tag{20}$$

$$r=|\mathbf{r}_{1c}-\mathbf{r}_{2c}|,$$

where $\rho_1$ and $\rho_2$ are the density distribution of projectile and target, respectively, $\mathbf{r}_{1c}$ and $\mathbf{r}_{2c}$ are their centers of mass, respectively. By using the QMD model, both the static and dynamic Coulomb barrier can be calculated. The static density distribution of the projectile and target is adopted for calculating the static Coulomb barrier, while the dynamical density distribution for fusion partners is adopted for the dynamic barrier. Therefore, for the static barrier the dynamical effects experienced by fusion partners during the reaction process are not taken into account. In this section we only discuss the static Coulomb barrier and leave the dynamical Coulomb barrier to be discussed in Sec. III C. Concerning the static density distribution, we let the initial projectile and

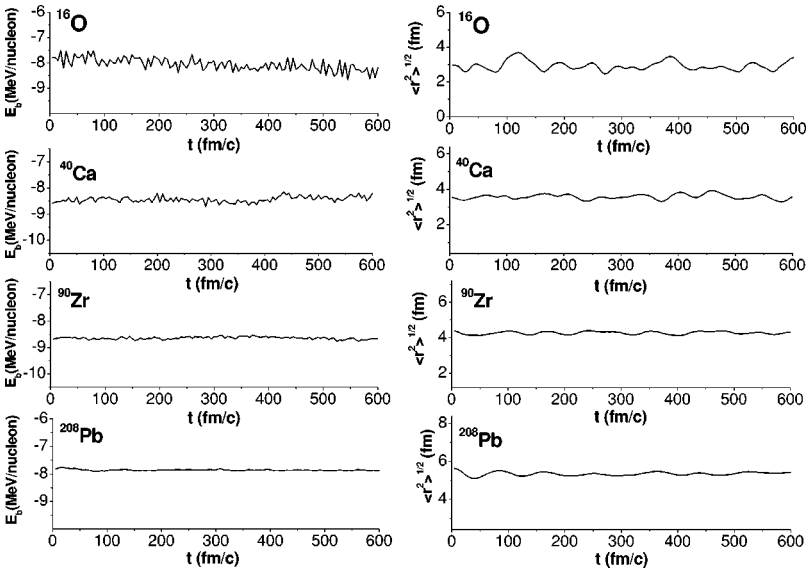


FIG. 7. The time evolution of the binding energies and the root-mean-square radii for ground states of $^{16}$O, $^{40}$Ca, $^{90}$Zr, and $^{208}$Pb.

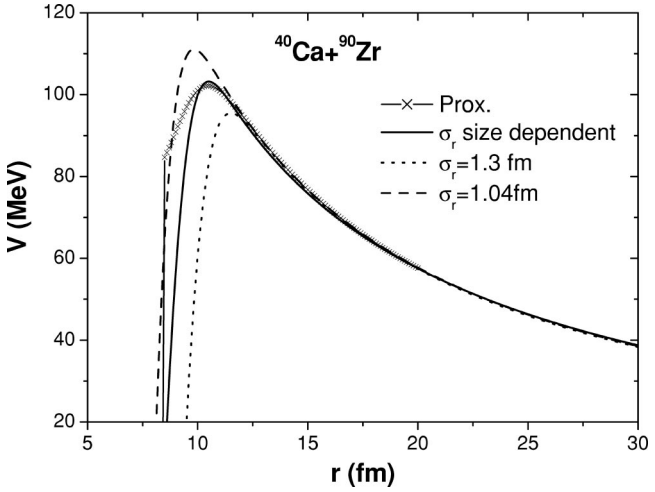


FIG. 8. The static Coulomb barrier for $^{40}$Ca+ $^{90}$Zr. The solid curve denotes the results with the system-size-dependent wave-packet width. The dotted and dashed curves denote the results with $\sigma_r = 1.3$ and 1.04 fm, respectively. The result of proximity potential is given by the crossed curve.

target nuclei evolve under their self-consistent mean fields individually for about 300 fm/$c$. Then we take the density distribution at this time as a static density distribution to calculate the Coulomb barrier. Figure 8 shows the average static Coulomb barrier for $^{40}$Ca+ $^{90}$Zr reactions. The solid curve denotes the results calculated with the system-size-dependent wave-packet width. The dotted and dashed curves denote the results calculated with a fixed wave-packet width $\sigma_r$ equal to 1.3 fm (adopted in [13]) and 1.04 fm (adopted in [10]), respectively. In order to make a comparison, in the figure we also show the result from the proximity potential [25] (the crossed curve). One can see that the Coulomb barrier calculated with our improved QMD model is in good agreement with that from the proximity potential [25], except in the case when two nuclei overlap in space. The reason for the deviation in the overlapping region is that the proximity potential is only applicable to the case when two nuclei are not overlapping, and may not be able to give an accurate result at the overlapping region. However, the Coulomb barriers calculated with a fixed width $\sigma_r$, taken to be 1.3 and 1.04 fm, are either too low or too high compared with a proximity potential. This figure indicates the importance of taking the system-size-dependent wave-packet width in describing the Coulomb barrier.

### C. Fusion reaction

After making the preparation of initial nuclei as mentioned in Sec. II D, we elaborately select ten projectile nuclei and ten target nuclei from thousands of preprepared systems. By rotating these prepared projectile and target nuclei around their centers of mass by a Euler angle chosen randomly, we create 100 bombarding events for each reaction energy $E$ and impact parameter $b$. Through counting the number of fusion events, we obtain the probability of fusion reaction $g_{fus}(E,b)$; then the cross section is calculated by using the expression

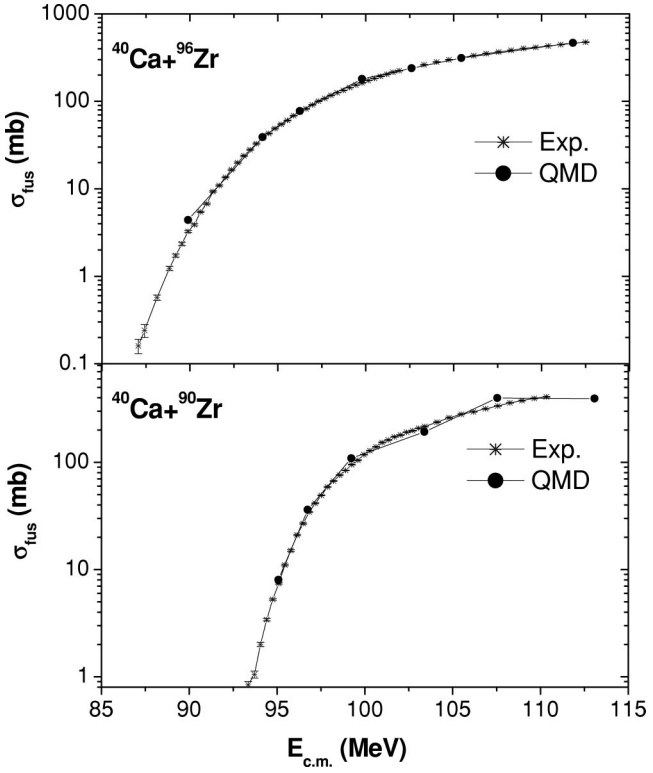


FIG. 9. The fusion cross sections for $^{40}$Ca+ $^{90,96}$Zr. The solid curves denote the results of this work and the crossed curves denote the experimental data (taken from Ref. [26]).

$$\sigma_{fus} = 2\pi \int_0^{b_{\max}} b g_{fus}(E,b)\,db = 2\pi \sum b g_{fus}(E,b)\Delta b. \tag{21}$$

The distance from projectile to target at initial time is taken to be $l = 20$ fm.

The definition of fusion in the QMD model is still a difficult problem which needs to consider carefully. In time-dependent Hartree-Fock (TDHF) calculations, the fusion event is defined rather operationally as the event in which the coalesced one-body density survives through one or more rotations of composite system or through several oscillations of its radius. In this work we also use the same definition of fusion event with that in TDHF calculations. In addition, considering the specific feature of QMD calculations, an event in which one or several nucleons escape prior to the formation of compound nucleus is still regarded as a fusion event [18]. Here we consider any event, for which the number of nucleons that escape during the process of forming compound nuclei is equal to or less than 6, a fusion event.

Figure 9 shows the fusion cross sections for (a) $^{40}$Ca + $^{90}$Zr and (b) $^{40}$Ca+ $^{96}$Zr, respectively. Experimental data are taken from Ref. [26]. One can see that our model prediction agrees with the experimental data remarkably well for both $^{40}$Ca+ $^{90}$Zr and $^{40}$Ca+ $^{96}$Zr cases. Neither adjusting parameters nor adding some special reaction channels for neutron-rich nuclear reactions (see Ref. [27]) are needed in our approach. This implies that our model is quite successful in describing neutron-rich nuclear fusion reactions near bar-

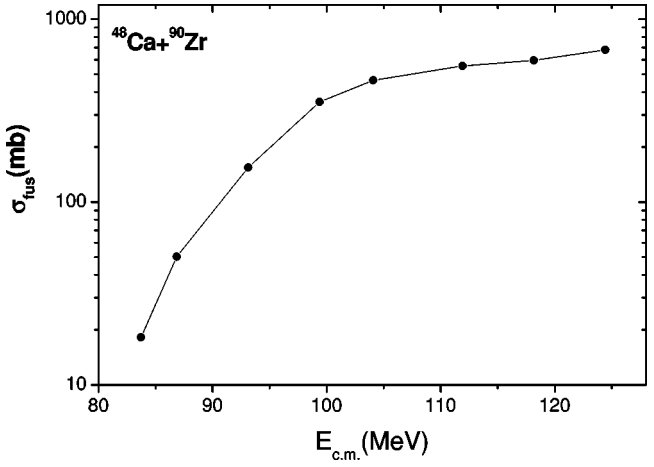


FIG. 10. The excitation function of fusion cross sections for $^{48}$Ca+ $^{90}$Zr.

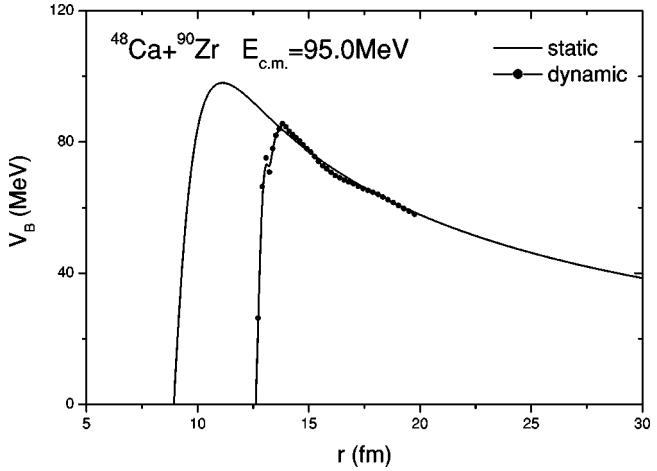


FIG. 11. The Coulomb barrier for fusion reaction $^{48}$Ca+ $^{90}$Zr at the energy $E_{\mathrm{c.m.}}=95.0$ MeV. The solid curve denotes the static Coulomb barrier and the solid curve with dots denotes the dynamic Coulomb barrier.

rier. To investigate the effect of neutron-rich projectile on fusion cross sections, we show the calculation results of fusion cross sections for $^{48}$Ca+ $^{90}$Zr in Fig. 10. From the comparison of the fusion cross sections for $^{40}$Ca+ $^{90}$Zr, $^{40}$Ca + $^{96}$Zr, and $^{48}$Ca+ $^{90}$Zr, one can easily find that there is a strong enhancement of fusion cross sections for neutron-rich nuclear reactions. In order to study the mechanism of the enhancement of fusion cross sections for neutron-rich nuclear reactions, we study the height of dynamic Coulomb barrier, the potential well of compound nuclei, and the neutron and proton density distributions of compound nuclei. Here the height of the dynamic Coulomb barrier means the height of the highest Coulomb barrier experienced in the path of fusion. The method for calculating the dynamic Coulomb barrier is given in Sec. III B. The potential well of a compound system is given by the expression

$$V_{com}(\mathbf{r}')=\int \rho_{com}(\mathbf{r})V(\mathbf{r}-\mathbf{r}')d^3\mathbf{r}, \tag{22}$$

where $\rho_{com}(\mathbf{r})$ is the density distribution of compound nuclei formed in fusion reactions, and $V(\mathbf{r}-\mathbf{r}')$ is the effective nucleon-nucleon interaction. The calculated results for $^{40}$Ca + $^{90}$Zr, $^{40}$Ca+ $^{96}$Zr, and $^{48}$Ca+ $^{90}$Zr at $E_{\mathrm{c.m.}}=95.0$ MeV (just below the barrier) and 107.6 MeV (above the barrier) are listed in Table III. One can find that the dynamical Coulomb barrier is energy dependent. The barrier lowering is stronger at 95 MeV than at 107.6 MeV. This feature of barrier lowering, i.e., the barrier lowering is most significant at energy near to the barrier height, was also observed in Ref. [7] for symmetric oxygen and nickel isotopes by means of the mean-field transport theory.

TABLE III. The height of the dynamic Coulomb barrier and the depth of the mean potential well of the compound nuclei in fusion reactions $^{40}$Ca+ $^{90}$Zr, $^{40}$Ca+ $^{96}$Zr, and $^{48}$Ca+ $^{90}$Zr at $E_{\mathrm{c.m.}}=95.0$ and 107.6 MeV, respectively.

| Fusion reaction | $E_{\mathrm{c.m.}}=95.0$ MeV | | $E_{\mathrm{c.m.}}=107.6$ MeV | |
|---|---|---|---|---|
| | $V_b$(MeV) | $V_{com.}$(MeV) | $V_b$(MeV) | $V_{com.}$(MeV) |
| $^{40}$Ca+ $^{90}$Zr | 85.2 | 44.97 | 88.1 | 44.92 |
| $^{40}$Ca+ $^{96}$Zr | 80.6 | 45.38 | 88.2 | 45.29 |
| $^{48}$Ca+ $^{90}$Zr | 84.4 | 45.21 | 85.4 | 45.03 |

Now let us study the effect of a neutron-rich target by comparing reactions $^{40}$Ca+ $^{90}$Zr and $^{40}$Ca+ $^{96}$Zr at energies near the barrier. For $^{40}$Ca+ $^{96}$Zr case, at $E_{\mathrm{c.m.}}=107.6$ MeV, the average height of the dynamic Coulomb barrier is about 88.2 MeV which is lower than that of the static Coulomb barrier (about 98.0 MeV), and the average depth of the mean potential well of compound nuclei $V_{com}$ is about 45.38 MeV. Comparing with the non-neutron-rich target case of $^{40}$Ca+ $^{90}$Zr, one can see that at this energy the height of the dynamic Coulomb barrier for both cases is almost equal, and the mean potential well of compound nuclei formed in $^{40}$Ca+ $^{96}$Zr is only about 0.3 MeV deeper than that in $^{40}$Ca+ $^{90}$Zr. But, as the energy decreases to $E_{\mathrm{c.m.}}=95.0$ MeV, the height of the dynamic Coulomb barrier for $^{40}$Ca+ $^{96}$Zr is about 80.6 MeV which is more than 5 MeV lower than that for the $^{40}$Ca+ $^{90}$Zr case. While the depth of the mean potential well of compound nuclei formed in the fusion process at this energy increases a little compared with that at $E_{\mathrm{c.m.}}=107.6$ MeV for both $^{40}$Ca+ $^{90}$Zr and $^{40}$Ca + $^{96}$Zr cases. From the above discussion, we find that the dynamic Coulomb barrier for the neutron-rich target case $^{40}$Ca+ $^{96}$Zr decreases much stronger than that for non-neutron-rich target case $^{40}$Ca+ $^{90}$Zr as the energy decreases from 107.6 to 95.0 MeV. Consequently, it leads to a stronger enhancement of the fusion cross sections for $^{40}$Ca+ $^{96}$Zr at lower energies.

Let us turn to the neutron-rich projectile case, $^{48}$Ca + $^{90}$Zr. Figure 11 shows a comparison between the static and dynamic Coulomb barrier for reaction $^{48}$Ca+ $^{90}$Zr at an energy of $E_{\mathrm{c.m.}}=95.0$ MeV. The solid curve denotes the static Coulomb barrier, and the solid curve with dots denotes the dynamic Coulomb barrier. One can see that in this case the dynamic Coulomb barrier is lower and thinner than the static Coulomb barrier. Concerning the height of the dynamic Cou-

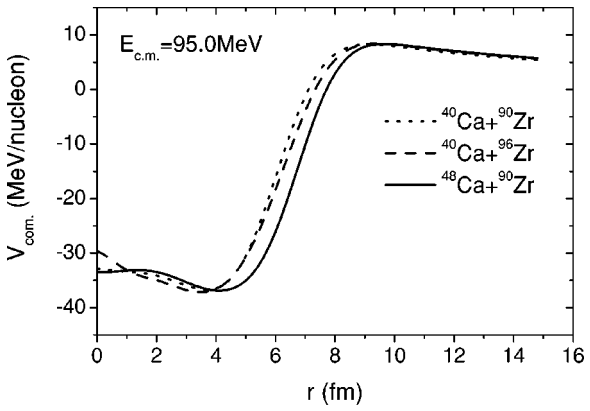


FIG. 12. The comparison between the mean potential wells of compound nuclei formed in fusion reactions $^{40}$Ca+ $^{90}$Zr, $^{40}$Ca + $^{96}$Zr, and $^{48}$Ca+ $^{90}$Zr. The dotted, dashed, and solid curves are for $^{40}$Ca+ $^{90}$Zr, $^{40}$Ca+ $^{96}$Zr, and $^{48}$Ca+ $^{90}$Zr, respectively.

lomb barrier, from Table III one can see that at the energy $E_{\mathrm{c.m.}}=107.6$ MeV, the height of the dynamic Coulomb barrier for $^{48}$Ca+ $^{90}$Zr is about 85.4 MeV, which is about 3 MeV lower than that for both $^{40}$Ca+ $^{90}$Zr and $^{40}$Ca+ $^{96}$Zr cases. At $E_{\mathrm{c.m.}}=95.0$ MeV, the height of the barrier falls about 1 MeV, and is lower than that for $^{40}$Ca+ $^{90}$Zr but higher than that for $^{40}$Ca+ $^{96}$Zr. The mean potential well of the compound nuclei formed in $^{48}$Ca+ $^{90}$Zr is a little deeper than that formed in $^{40}$Ca+ $^{90}$Zr. On the other hand, the shape of the mean potential well formed in the fusion process may also influence the fusion probability. In Fig. 12 we show the mean potential wells of compound nuclei formed in $^{40}$Ca + $^{90}$Zr (the dotted curve), $^{40}$Ca+ $^{96}$Zr (the dashed curve), and $^{48}$Ca+ $^{90}$Zr (the solid curve). One can find that the mean potential well of compound system formed in $^{48}$Ca+ $^{90}$Zr is obviously wider than the other two cases. And when energy decreases from $E_{\mathrm{c.m.}}=107.6$ MeV to $E_{\mathrm{c.m.}}=95.0$ MeV, the depth of the mean potential well of compound nuclei formed in $^{48}$Ca+ $^{90}$Zr increases more than the other two cases (see Table III). In order to understand the reason for forming the different mean potential wells in these three different reactions, we show the neutron and proton density distributions of compound nuclei for three cases in Fig. 13. From this figure one can see that the proton distribution for reaction $^{48}$Ca+ $^{90}$Zr is more suitable for forming a more stable compound nuclei. This kind of density distribution seems to have the advantage of forming a favorable potential well which may lead to an enhancement of fusion cross sections.

From the above discussion we can attribute the mechanism of the enhancement of fusion cross sections for reactions with a neutron-rich target or projectile, $^{40}$Ca+ $^{96}$Zr $^{48}$Ca+ $^{90}$Zr, to gaining a larger dynamical barrier lowering, or forming a more favorable potential well of a compound system, or both. However, as soon as the two nuclei approach each other, their shapes can be deformed and, after contact, a neck will develop, which will lead to barrier lowering. What is the role played by the excess neutrons in a neutron-rich projectile and target in this dynamical process? How do protons and neutrons transfer during the fusion process? All these problems are very important for further understanding the mechanism of the enhancement of the fusion cross section. They will be studied in our future work.

## IV. CONCLUSION

In this work, we have developed an improved QMD model. The improvements mainly include introducing the system-size-dependent wave packet width and taking into account the effects of the surface term and the phase-space density constraint. By using this model the ground-state properties, including binding energies, root-mean-square radii, density distributions, and momentum distributions, as well as their time evolution for selected nuclei from $^{6}$Li to $^{208}$Pb, have been described very well with one set of parameters. The Coulomb barrier has also been described well, and the experimental data of the fusion cross sections for $^{40}$Ca + $^{90,96}$Zr have been reproduced remarkably well without introducing any new parameters. In addition, the fusion reactions for $^{48}$Ca+ $^{90}$Zr at energies near barrier have been studied. The mechanism for the enhancement of fusion cross sections for neutron-rich nuclear reaction near a barrier has been analyzed and attributed to a larger dynamic lowering of the Coulomb barrier, or a more favorable potential well of a compound system formed in a fusion process, or both. Nevertheless, the problems concerning the neck dynamics and the mass transfer have not been discussed in this paper. Work about these aspects is in progress.

## ACKNOWLEDGMENTS

Supported by the National Natural Science Foundation of China under Grant Nos. 19975073, 10175093, and 10175089, and by the Science Foundation of Chinese Nuclear Industry and Major State Basic Research Development Program under Contract No. G20000774.

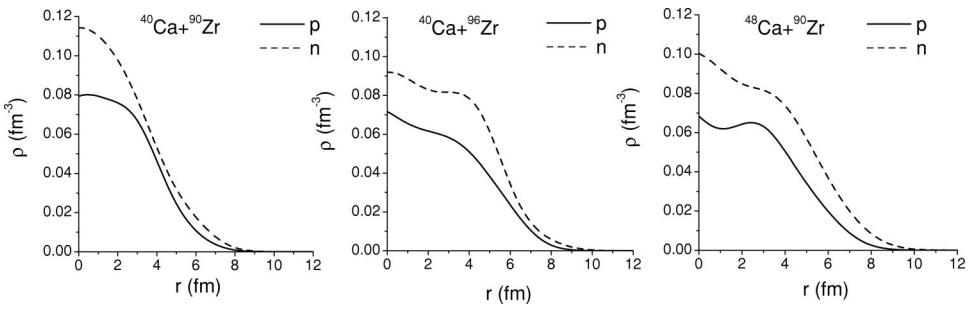


FIG. 13. The density distributions of compound nuclei formed in $^{40}$Ca+ $^{90}$Zr, $^{40}$Ca+ $^{96}$Zr, and $^{48}$Ca+ $^{90}$Zr. The dashed and solid curves denote the neutron and proton density distributions, respectively.

[1] M. Beckerman, Phys. Rep. **129**, 145 (1985); Rep. Prog. Phys. **51**, 1047 (1988).
[2] R. Vandenbosch, Annu. Rev. Nucl. Part. Sci. **44**, 447 (1992).
[3] W. Reisdorf, J. Phys. G **20**, 1297 (1994).
[4] A.B. Balantekin and N. Takigawa, Rev. Mod. Phys. **70**, 77 (1998).
[5] *Proceedings of the International Workshop on Heavy Ion Collisions at Near Barrier Energies* [J. Phys. G **23** 1157 (1997)].
[6] K. Hagino, N. Takigawa, M. Dasgupta, D.J. Hinde, and J.R. Leigh, Phys. Rev. Lett. **79**, 2014 (1997); K. Hagino, N. Takigawa, and S. Kuyucak, *ibid.* **79**, 2943 (1997).
[7] V.N. Kondratyev, A. Bonasera, and A. Iwamoto, Phys. Rev. C **61**, 044613 (2000).
[8] Ch. Hartnack, Zhuxia Li, L. Neise, G. Peilert, A. Rosenhauser, H. Sorge, J. Aichelin, H. Stoecker, and W. Greiner, Nucl. Phys. **A495**, 303 (1989).
[9] J. Aichelin, Phys. Rep. **202**, 233 (1991), and references therein.
[10] Ch. Hartnack, Rajeev K. Puri, and J. Aichelin, Eur. Phys. J. A **1**, 151 (1998).
[11] A. Ono, H. Horiuchi, Toshiki Maruyama, and A. Ohnishi, Phys. Rev. Lett. **68**, 2898 (1992); Y. Kanada-En'yo and H. Horiuchi, Phys. Rev. C **52**, 647 (1995); Y. Kanada-En'yo, H. Horiuchi, and A. Doté, *ibid.* **60**, 064304 (1999).
[12] H. Feldmeier and J. Schneck, Prog. Part. Nucl. Phys. **39**, 392 (1997), and references therein.
[13] Massimo Papa, Toshiki Maruyama, and Aldo Bonasera, Phys. Rev. C **64**, 024612 (2001).
[14] David H. Boal and James N. Glosi, Phys. Rev. C **37**, 91 (1988); **38**, 2621 (1988).
[15] L. Wilets *et al.*, Nucl. Phys. **A282**, 341 (1977).
[16] C.O. Dorso *et al.*, Phys. Lett. B **188**, 287 (1987).
[17] Zhuxia Li, Ch. Hartnack, H. Stoecker, and W. Greiner, Phys. Rev. C **40**, 824 (1991).
[18] T. Maruyama *et al.*, Phys. Rev. C **57**, 655 (1998).
[19] Toshiki Maruyama, K. Niita, and A. Iwamoto, Phys. Rev. C **53**, 297 (1996).
[20] Toshiki Maruyama, Aldo Bonasera, Massimo Papa, and Satoshi Chiba, nucl-th/0107021.
[21] D. Vautherin and D.M. Brink, Phys. Rev. C **5**, 626 (1972).
[22] Qingfeng Li and Zhuxia Li, Phys. Rev. C **64**, 064612 (2001).
[23] P.G. Reinhard, M. Rufa, J. Maruhu, W. Greiner, and J. Fridrich, Z. Phys. A **323**, 13 (1986).
[24] M. A. Preston and R. K. Bhaduri, *Structure of the Nucleus* (Addison-Wesley, Reading, MA, 1975), pp. 10–14.
[25] W.D. Myers and W.J. Swiatecki, Phys. Rev. C **62**, 044610 (2000).
[26] H. Timmers, D. Ackermann, S. Beghini, L. Corradi, J.H. He, G. Montagnoli, F. Scarlassara, A.M. Stefanini, and N. Rowley, Nucl. Phys. **A633**, 421 (1998).
[27] V.Yu. Denisov, nucl-th/9809083.